nature communications

Article

https://doi.org/10.1038/s41467-025-58062-4

Robust super-structured porous hydrogel enables bioadaptive repair of dynamic soft tissue

Received: 9 September 2024

Accepted: 11 March 2025

Published online: 03 April 2025

Check for updates

Siqi He[1,5], Weiwen Liang[2,5], Youchen Tang[3,5], Jinquan Zhang[1], Runxian Wang[1], Luna Quan[4], Yang Ouyang[2], Rongkang Huang[2] ✉, Ruoxu Dou[1] ✉ & Dingcai Wu[4] ✉

Well-orchestrated integration of multiple contradictory properties into a single material is crucial for dynamic soft tissue defect repair but remains challenging. Bioinspired by diaphragm, we have successfully developed a robust super-structured porous hydrogel with anisotropic skeleton and asymmetric porous surfaces via integrated molding. Thanks to synergistic toughening of anisotropic structure and Hofmeister effect of amino acid, our hydrogel achieves high tensile strength (22.2 MPa) and elastic modulus (32.4 MPa) for strong mechanical support, while maintaining excellent toughness (61.9 MJ m^{-3}) and fatigue threshold (5.6 kJ m^{-2}) against dynamic stretching during the early healing phase. The mechanical properties of hydrogel gradually decrease during the late healing phase, minimizing its restriction on physiological movements. In addition, diaphragm defect repair models on female rabbits demonstrate asymmetric porous surfaces can simultaneously prevent visceral adhesion and promote defect healing. Therefore, our hydrogel opens an attractive avenue for the construction of biomimetically hierarchical materials to address the stringent requirements of dynamic tissue defect repair.

Dynamic soft tissues undertake a variety of physiological movements that are essential for maintaining life, including arterial pulsation, diaphragmatic respiration, and intestinal peristalsis. The successful completion of these intricate physiological movements relies on the precise coordination of multidimensional mechanical and biological performances of dynamic soft tissues[1–4]. Despite their diversity, dynamic soft tissues share some common structural features[5,6]. For example, a mechanical support layer containing anisotropic muscle fibers exhibits excellent strength and fatigue resistance for ceaseless physiological movements while maintaining adequate stretchability; asymmetric layers located on two sides of the mechanical support layer fulfill different biological functions[7–12]. These characteristics highlight that trade-offs are critical in the properties of repair materials for dynamic soft tissue defect, including balancing sufficient stiffness for local mechanical support and high toughness for physiological stretching[13–16], as well as integrating asymmetric bioadhesive surfaces for wound pro-healing and visceral anti-adhesion[17,18]. Furthermore, their mechanical properties should optimally accommodate the dynamic healing process[19–21]. With the regeneration of defective tissues, the initially robust mechanical properties should gradually

[1]Department of Gastrointestinal Surgery, The Fifth Affiliated Hospital, Sun Yat-sen University, Zhuhai 519000, P. R. China. [2]Department of General Surgery (Colorectal Surgery), Guangdong Institute of Gastroenterology, Guangdong Provincial Key Laboratory of Colorectal and Pelvic Floor Diseases, The Sixth Affiliated Hospital, Sun Yat-sen University, Guangzhou 510655, P. R. China. [3]The Eighth Affiliated Hospital, Sun Yat-sen University, Shenzhen 518033, P. R. China. [4]Key Laboratory for Polymeric Composite and Functional Materials of Ministry of Education, School of Chemistry, Sun Yat-sen University, Guangzhou 510006, P. R. China. [5]These authors contributed equally: Siqi He, Weiwen Liang, Youchen Tang. ✉e-mail: huangrk3@mail.sysu.edu.cn; dourx@mail.sysu.edu.cn; wudc@mail.sysu.edu.cn

decrease to facilitate the restoration of unrestricted physiological movements[13,22,23].

Conventional hydrogels with high water contents and loose crosslinking usually have limited mechanical properties for solving the physiological movements of dynamic soft tissues[24–26]. Recently, various technologies such as freezing-thawing[27], solvent-exchange[28], salting out[29], and annealing[30] have been used to alter the polymer aggregation states to improve the mechanical performances of hydrogels. On the other hand, natural hierarchical structures are widely imitated to design multifunctional hydrogels with contradictory mechanical and biological properties, such as high strength and high toughness, as well as adhesion and anti-adhesion[2,4,31–33]. However, most multifunctional hydrogels with hierarchical structures consist of double or multiple networks[15,34,35], and adjusting their polymer aggregation states to meet the mechanical requirements of the dynamic healing process is complicated. Therefore, to design single-network hydrogels with hierarchical structures and comprehensive mechanical properties that match specific biological tissues, manipulating the spatiotemporal expression of interactions between polymer chains during the "network construction" and "polymer dissociation" processes of hydrogels may provide a promising way but remains a formidable challenge.

Herein, bioinspired by a typical dynamic tissue (i.e., diaphragm), we have developed a robust super-structured porous hydrogel for the repair of dynamic soft tissue defect. By directional freezing-assisted progressive solvent exchange process, the biomimetically structured hydrogel with anisotropic skeleton and asymmetric porous surfaces is constructed in an integrated manner. According to conceptions of eutectic solvent and cononsolvency effect[36,37], the thawing rate of the frozen template is effectively reduced and sufficient hydrogen bonds between polymer chains are formed before the template disappears in our progressive solvent exchange method, leading to the maintenance of anisotropic skeleton. The subsequent Hofmeister effect of amino acid significantly enhances the aggregation of polymer chains to form robust networks in hydrogel. Due to the synergistic toughening of anisotropic skeleton and Hofmeister effect of amino acid, our hydrogel can achieve high tensile strength (22.2 MPa) and high elastic modulus (32.4 MPa) to provide strong mechanical support, while maintaining excellent toughness (61.9 MJ m^{-3}) and high fatigue threshold (5.6 kJ m^{-2}) to tolerate ceaseless physiological stretching during the early healing phase of dynamic tissue defect. Moreover, hydrophobic modification can slow down the disgregation of hydrogel networks in a wet environment by retarding the absorption of water. As a result, our hydrogel exhibits bioadaptive changes in tensile strength and elastic modulus, which can effectively maintain mechanical support and minimize the restriction of repair materials on physiological movements during the late healing phase. Benefiting from the asymmetric porous surfaces, our hydrogel can prevent visceral adhesion based on its dense porous surface while promoting defect healing based on its loose porous surface in the rabbit diaphragm defect repair model. Therefore, our strategy for the construction of robust super-structured hydrogels provides an attractive avenue for the development of biomimetic materials for dynamic soft tissue engineering.

Results and Discussion

Synthesis of HAA-SPVA hydrogel

It is known that the construction of materials' nano-micro-macro multiscale structures often requires the combination of complex processing techniques. As shown in Fig. 1, the feasibility of our integrated molding method is demonstrated by using a robust super-structured porous hydrogel (hydrophobic and amino acid-toughened super-structured polyvinyl alcohol (HAA-SPVA) hydrogel) as a conceptual example. The design of HAA-SPVA hydrogel is inspired by the natural diaphragm, which has a highly ordered hierarchical structure, including an anisotropic muscle fiber skeleton for incessant respiratory movements, a dense abdominal surface for visceral adhesion prevention, and a loose mediastinal surface for cushioning protection (Fig. 2a,b)[38,39]. For the preparation of HAA-SPVA hydrogel, the PVA/dimethyl sulfoxide (DMSO) solution firstly undergoes directional freezing to construct an anisotropic structure. The high freezing temperature (18 °C) of DMSO makes it easier for PVA/DMSO solution to form anisotropic PVA/DMSO frozen solid at −25 °C, instead of the ultra-low temperature (normally below −60 °C) required by the traditional ice template method (Supplementary Fig. 1)[4,40–46]. Subsequently, the anisotropic PVA/DMSO frozen solid is vertically placed along the freezing direction and exposed to cold moisture at −20 °C for a top-down progressive solvent exchange (Supplementary Fig. 2). Due to the strong interaction between DMSO and water molecules, moisture could be gradually sorbed on the surface of the PVA/DMSO frozen solid and thaw the frozen DMSO to form a DMSO/water eutectic solvent with a depressed freezing temperature. This process simultaneously triggers the progressive removal of the directionally frozen DMSO template, the formation of hydrogen bond networks between PVA chains via cononsolvency effect, and the dissolution of partial PVA chains on the top surface, leading to an interesting integrated molding of a super-structured porous PVA (SPVA) hydrogel with anisotropic skeleton and asymmetric porous surfaces after hydration (Fig. 2c, d). The top surface of freeze-dried SPVA exhibits a loose porous structure with pore sizes ranging from 1.81 to 5.94 μm, which is similar to extracellular matrix and conducive to cell adhesion and proliferation[47,48], while the bottom surface exhibits a dense porous structure with pore sizes ranging from 0.38 to 0.99 μm (Supplementary Fig. 3). By contrast, when hydrophobic sellotape is used to cover the top surface of the PVA/DMSO frozen solid, the multiscale structure of SPVA hydrogel could not be constructed due to the obstruction of progressive solvent exchange process (Fig. 2e). As shown in Fig. 2f,g, there is a noticeable liquid PVA/DMSO/H_2O mixture on the top surface of SPVA organogel after exposure to cold moisture for 24 h, and the freezing temperature ultimately decreases from initially 18 °C for DMSO to below −60 °C for PVA/DMSO/H_2O mixture collected after 72 h, demonstrating the significant depression in freezing temperature triggered by the combination of DMSO and H_2O[37]. Furthermore, the anisotropic structures of SPVA hydrogel are impaired by aggravating the solvent exchange process with an increase of environmental temperature (Fig. 2h and Supplementary Fig. 4). It could be explained that the low ambient temperature reduces the thawing rate of the frozen DMSO template and facilitates the formation of hydrogen bonds between PVA chains. Sufficient hydrogen bonds are formed between PVA chains via the solvent exchange process before the template disappears, resulting in the maintenance of anisotropic structure[49,50]. The feasibility of this method is further demonstrated by another super-structured porous hydrogel based on gelatin (Supplementary Fig. 5). Finally, SPVA hydrogel is immersed in amino acid solution (such as serine) after freeze-drying to enhance its mechanical performances through the Hofmeister effect[51,52], producing amino acid-toughened SPVA (AA-SPVA) hydrogel, and further hydrophobically modified with long-chain alkylation to slow down its mechanical withdrawal in the wet environment, eventually yielding our HAA-SPVA hydrogel.

Characterization of mechanical properties

During the early healing phase of dynamic tissue defect, it is crucial for repair materials to balance adequate stiffness for local mechanical support with toughness for necessary physiological stretching[20,53]. However, a trade-off always exists between stiffness and toughness for bioengineering materials[14,15,54]. For example, commercial materials widely used in clinical practice (e.g., polyester) have high tensile strength but excessive stiffness (>1 GPa) and poor strain (<100%)[55–57], while most hydrogels have high water contents and stretchability but

https://doi.org/10.1038/s41467-025-58062-4

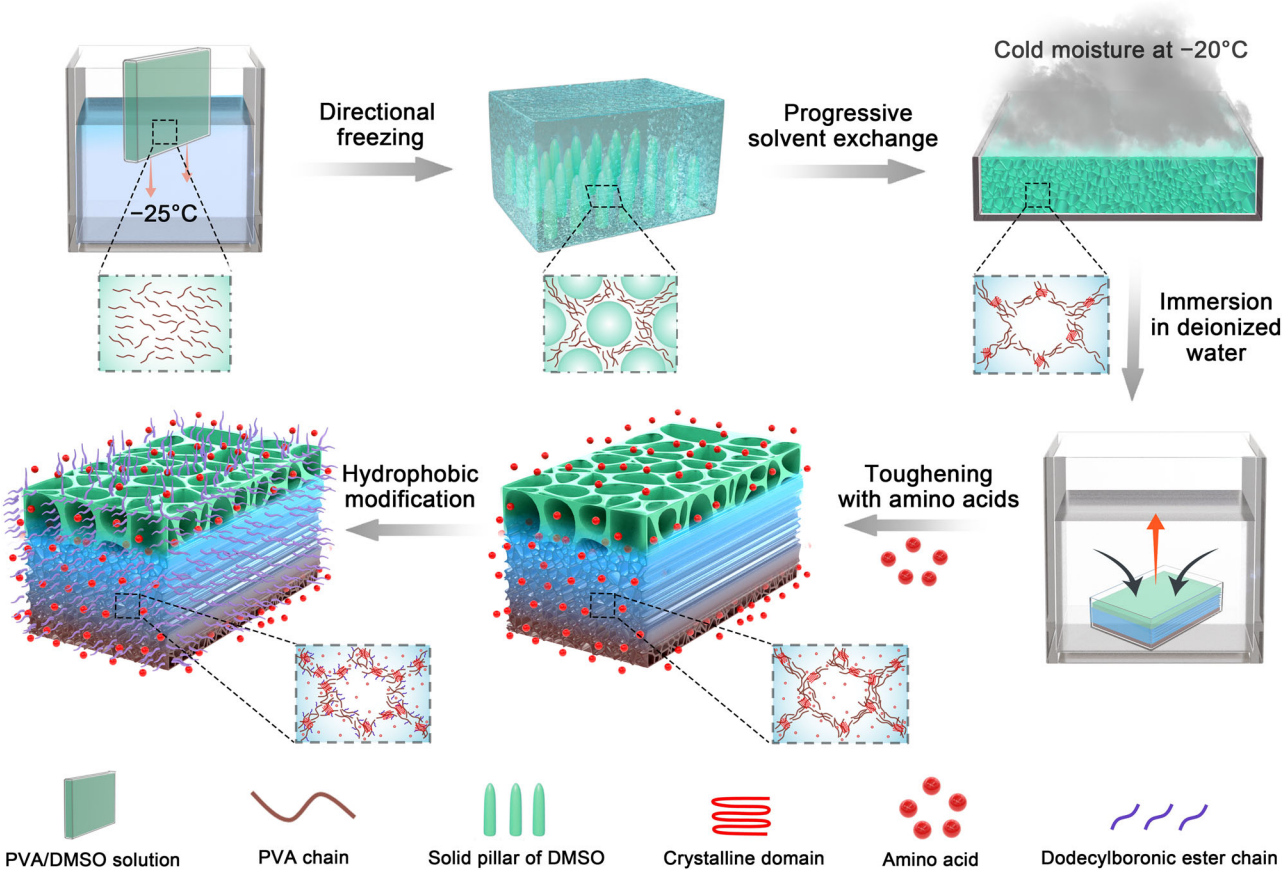

Fig. 1 | Construction and structure of HAA-SPVA hydrogel. Schematic illustration for preparation, morphological evolution, and formation of strong hydrogen bond networks for a robust super-structured porous hydrogel towards the repair of dynamic soft tissue defect. Directional freezing-assisted progressive solvent exchange process in cold moisture at −20 °C results in the biomimetic structure of anisotropic skeleton and asymmetric porous surfaces. The subsequent immersion of amino acid markedly enhances polymer chains aggregation to form robust networks, and immersion of dodecylboronic acid for hydrophobic modification slows down the disgregation of the networks in the wet environment, eventually providing our hydrogel with ultra-high and dynamic bioadaptive mechanical properties.

low strength and fatigue resistance[24,25]. Compared with SPVA and AA-SPVA hydrogels, the tensile strength and elastic modulus of HAA-SPVA hydrogel can reach exceptional 22.2 MPa and 32.4 MPa, respectively (Fig. 3a and Supplementary Fig. 6a, b), indicating efficient robustness against adverse tension caused by soft tissue movements[13]. Meanwhile, the toughness and fracture strain of HAA-SPVA hydrogel is as high as 61.9 MJ m^{-3} and 446%, respectively (Supplementary Fig. 6c,d). These robust mechanical properties enable HAA-SPVA hydrogel at a cross-section of 0.24 mm^2 to stably withstand a load of 5 kg in vitro (Supplementary Fig. 7). In terms of the strength, elastic modulus, and toughness, HAA-SPVA hydrogel is superior to many previously reported strong and tough hydrogels, natural rubber, and human dynamic soft tissues (e.g., aorta and small intestine) (Fig. 3b, c)[4,30,33,40,43,58–71]. Furthermore, the fatigue threshold of HAA-SPVA hydrogel can reach up to 5.6 kJ m^{-2} (Fig. 3d and Supplementary Fig. 8), which is better than that of many reported hydrogels (e.g., 0.3–2.7 kJ m^{-2}, normally <1 kJ m^{-2}, Fig. 3e)[30,41–43,62,64,72–76], suggesting that HAA-SPVA hydrogel has stable mechanical performance to tolerate the ceaseless physiological stretching of dynamic soft tissues. It has been reported that the mechanical properties of common human dynamic soft tissues such as diaphragm, small intestine, aorta, and abdominal wall can reach high tensile strength of 7.6 MPa, tensile modulus of 5.3 MPa, fracture strain of 180% (Supplementary Table 1), and fatigue threshold of 1 kJ m^{-2} [77,78]. The mechanical properties of HAA-SPVA hydrogel comprehensively exceed those of common dynamic soft tissues (Fig. 3f), demonstrating that our hydrogel can be customized to meet the needs of a wide variety of dynamic soft tissues. Therefore, during the early healing phase of dynamic tissue defect, HAA-SPVA hydrogel could provide strong mechanical support, while tolerating ceaseless physiological stretching.

During the late healing phase when dynamic tissue regrows and remodels, the initially strong mechanical properties of repair material should gradually give way to release its restriction on physiological movements, thus allowing the functional recovery of dynamic soft tissue[19–21]. To meet the unique mechanical requirements for initial robustness and gradual decline, AA-SPVA hydrogel was hydrophobically modified using dodecylboronic acid (Supplementary Fig. 9). After soaking in phosphate buffer saline (PBS), the tensile strength of HAA-SPVA hydrogel decreases from initial 22.2 MPa to 17.4, 10.0, and 8.5 MPa on the 1st, 14th, and 30th days, respectively (Fig. 3g), while that of AA-SPVA hydrogel dramatically decreases from 23.1 to 3.0 MPa on the 1st day (Supplementary Fig. 10). This relatively slow biomechanical withdrawal is achieved by hydrophobicity which retards the absorption of water (Supplementary Fig. 11). Meanwhile, the elastic modulus of HAA-SPVA hydrogel decreases from initial 32.4 MPa to 4.5 MPa after soaking in PBS for 14 days, resembling the modulus of common dynamic soft tissues (Fig. 3f, h). The HAA-SPVA hydrogel soaked in PBS for 14 days also shows good resilience under cyclic tensile test (Supplementary Fig. 12), which contributes to the recovery of unrestricted physiological movements. Thus, HAA-SPVA hydrogel could adapt to the healing process of dynamic soft tissues via timely changes in biomechanical properties.

The effect of the multiscale toughening approaches on our robust hydrogels was investigated. It's known that robust hydrogels can be

https://doi.org/10.1038/s41467-025-58062-4

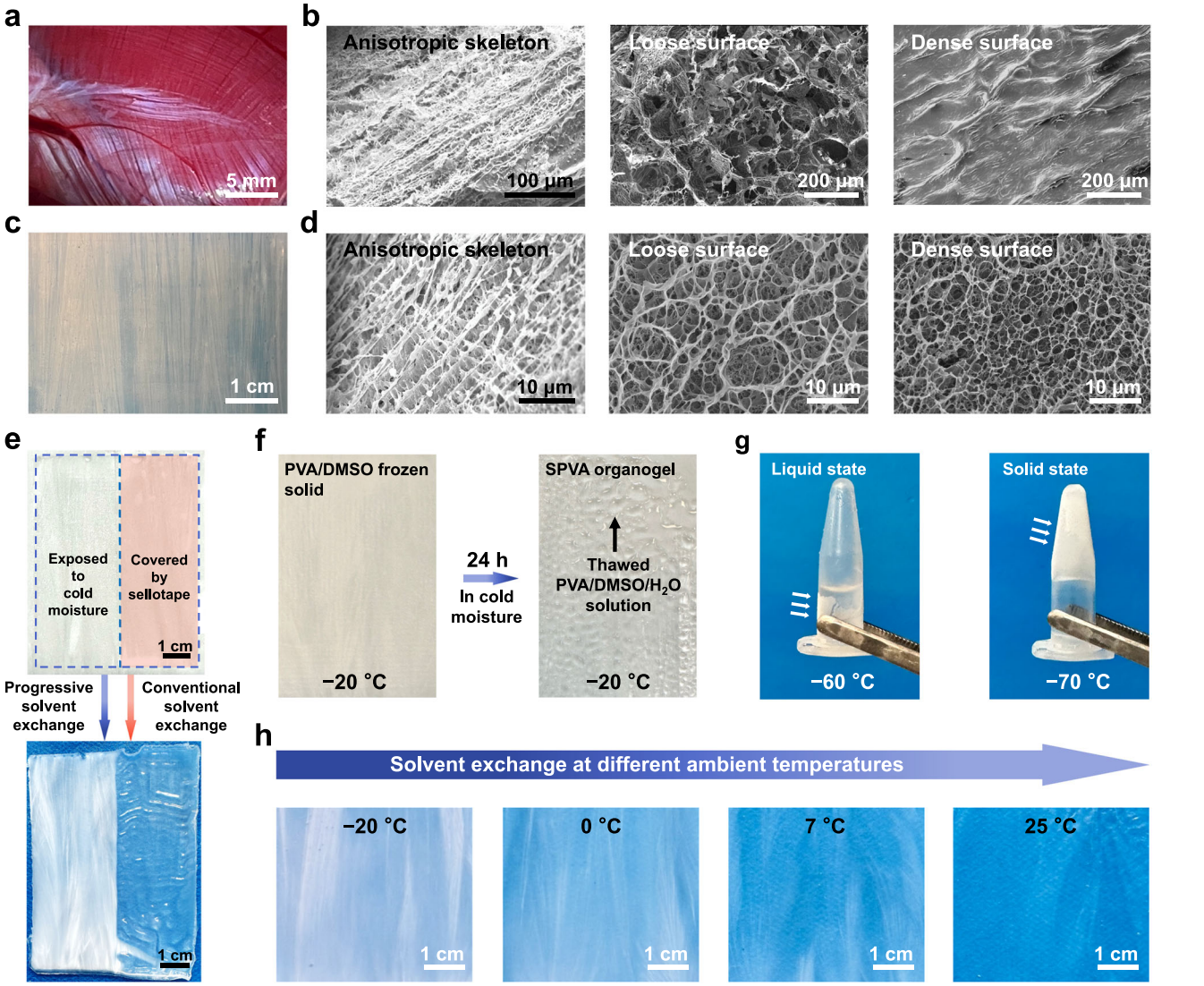

Fig. 2 | Morphology and formation mechanisms of SPVA hydrogel. a–d Macroscopic photos of natural diaphragm (**a**) and SPVA hydrogel (**c**), and scanning electron microscopy (SEM) images of freeze-dried natural diaphragm (**b**) and freeze-dried SPVA (**d**). SEM observation was repeated three times independently, yielding similar results. **e** Distinct macroscopic features of SPVA hydrogel with (left) or without (right) cold moisture exposure where half surface of the PVA/DMSO frozen solid is covered by sellotape. **f** Transformation from PVA/DMSO frozen solid into SPVA organogel containing thawed PVA/DMSO/H_2O solution on its top surface after a 24 h progressive solvent exchange at −20 °C. **g** The freezing temperature analysis of the thawed PVA/DMSO/H_2O solution after a 72 h progressive solvent exchange at −20 °C. **h** Macroscopic photos of SPVA hydrogel obtained by solvent exchange at different ambient temperatures of −20 °C, 0 °C, 7 °C, and 25 °C after directional freezing.

constructed through the Hofmeister effect of specific ions[29,52]. Immersion in salt solution has been widely used to enhance the mechanical properties of hydrogels[4,40,79–81], but the effective concentration of salt solution is generally required to be high, which is harmful to human health and difficult to be used in bioengineering[82]. Here, we find that biocompatible amino acids, important components of the human body, can enhance the mechanical properties of our hydrogel through the Hofmeister effect (Fig. 4a). SPVA hydrogel shrinks significantly after immersion in specific amino acid solutions (e.g., serine, lysine, glycine, arginine, and alanine) (Fig. 4b and Supplementary Fig. 13a), and its elastic modulus is remarkedly increased (Supplementary Fig. 13b). Considering the strong toughening effect and biofriendly pH value (Supplementary Fig. 13c), the serine solution is used to prepare AA-SPVA hydrogel. With serine toughening, the mechanical properties of SPVA can be greatly enhanced (Fig. 3a). Moreover, the anisotropic skeleton is conducive to local preconcentration of polymer chains to further enhance the mechanical properties and fatigue resistance[4]. Compared with AA-SPVA hydrogel (perpendicular to the alignment) and amino acid-toughened isotropic PVA (AA-IPVA) hydrogel, AA-SPVA hydrogel (parallel) shows superior tensile strength (3.5 and 1.6 times, respectively) and fracture strain (6.4 and 2.5 times, respectively) (Fig. 4c), demonstrating the unique synergistic toughening of amino acid and anisotropic skeleton.

As the main crosslinking points, crystallites play an important role in determining the mechanical properties of PVA gel[4,15]. To further quantify the evolution of crystallites during the toughening processes of HAA-SPVA hydrogel, a series of experiments were conducted. The results of 2D small-angle X-ray scattering (SAXS) (Fig. 4d) show the largest scattering circle of HAA-SPVA hydrogel, demonstrating the most significant phase separation caused by crystallization[83]. No peak is found in the 1D-SAXS curves of isotropic PVA (IPVA) hydrogel, whereas SPVA, AA-SPVA, and HAA-SPVA hydrogels show obvious peaks[67]. The corresponding distances between crystalline domains for SPVA, AA-SPVA, and HAA-SPVA hydrogels are 14.4, 8.4, and 9.4 nm,

https://doi.org/10.1038/s41467-025-58062-4

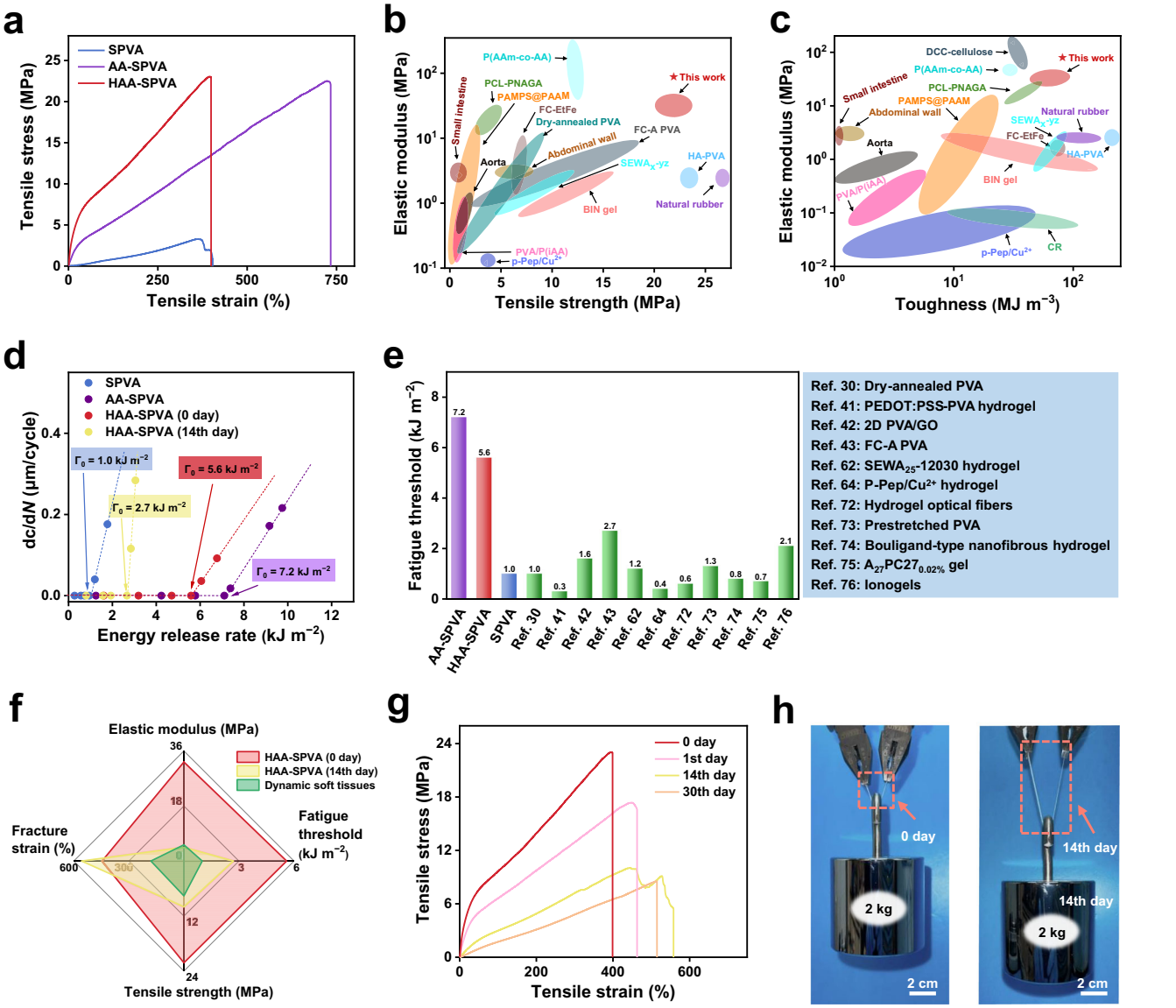

Fig. 3 | Biomechanical performances of SPVA, AA-SPVA, and HAA-SPVA hydrogels. a Tensile stress-strain curves of SPVA, AA-SPVA, and HAA-SPVA hydrogels. **b**, **c** Ashby diagrams of elastic modulus versus tensile strength (**b**) and elastic modulus versus toughness (**c**) of HAA-SPVA hydrogel, reported strong and tough hydrogels, and human dynamic soft tissues. **d** Crack growth rate (d*c*/d*N*) and the calculated energy release rate of SPVA, AA-SPVA, and HAA-SPVA hydrogels soaked in PBS for 0 and 14 days. The fatigue threshold is the critical energy release rate. **e** Comparison of SPVA, AA-SPVA, and HAA-SPVA hydrogels with the reported anti-fatigue hydrogels in terms of fatigue threshold. **f** Comparison of elastic modulus, fracture strain, tensile strength, and fatigue threshold between dynamic soft tissues and HAA-SPVA hydrogel soaked for 0 and 14 days. **g** Tensile stress-strain curves of HAA-SPVA hydrogel on the 0, 1st, 14th, and 30th days after soaking in PBS. **h** Photos of HAA-SPVA hydrogel soaked for 0 and 14 days with same cross-section and initial length lifting a 2 kg weight.

respectively (Fig. 4e, g), indicating higher crystalline density brought by amino acid. In addition, the wide-angle X-ray scattering (WAXS) curves (Fig. 4f) show obvious crystalline reflections at 2θ = 19.2°, corresponding to the typical reflection surface (101) of PVA[30]. The sizes of crystalline domain of IPVA, SPVA, AA-SPVA, and HAA-SPVA hydrogels are estimated to be 5.9, 6.8, 6.7, and 7.3 nm, respectively (Fig. 4f, g and Supplementary Fig. 14). As shown in the attenuated total reflection Fourier transform infrared (ATR-FTIR) spectra (Fig. 4h), the peak at 1140 cm^{-1} representing the fingerprint of the crystallinity for PVA confirms similar results during the toughening process[62,84]. The increase of crystalline domain density is also evident from the gradual decrease in water contents from SPVA to HAA-SPVA hydrogels (Supplementary Fig. 15). These results demonstrate that the crystalline domain density and the individual crystalline domain size of HAA-SPVA hydrogel are significantly increased by our toughening strategy. Therefore, the anisotropic structure with molecular tougheners enables PVA chains to highly aggregate and crystallize, efficiently promoting the excellent mechanical performances of HAA-SPVA hydrogel.

HAA-SPVA hydrogel for dynamic soft tissue repair

Excellent biocompatibility is the first challenge for the application of strong and tough hydrogels in bioengineering. The biocompatibility was evaluated by cytotoxicity experiments in vitro and subcutaneous implantation experiment in vivo. As shown in the fluorescence images of live/dead assay (Fig. 5a) and quantitative analysis of cell counting kit-8 (CCK-8) assay (Fig. 5b), L929 fibroblasts incubated without and with HAA-SPVA hydrogel show similar cell morphology and proliferation on the 1st, 2nd, and 3rd days, indicating good in vitro biocompatibility of HAA-SPVA hydrogel. After 14 days of subcutaneous implantation in rats, hematoxylin-eosin (HE) staining images show that both the control and HAA-SPVA hydrogel groups have few inflammatory cells

https://doi.org/10.1038/s41467-025-58062-4

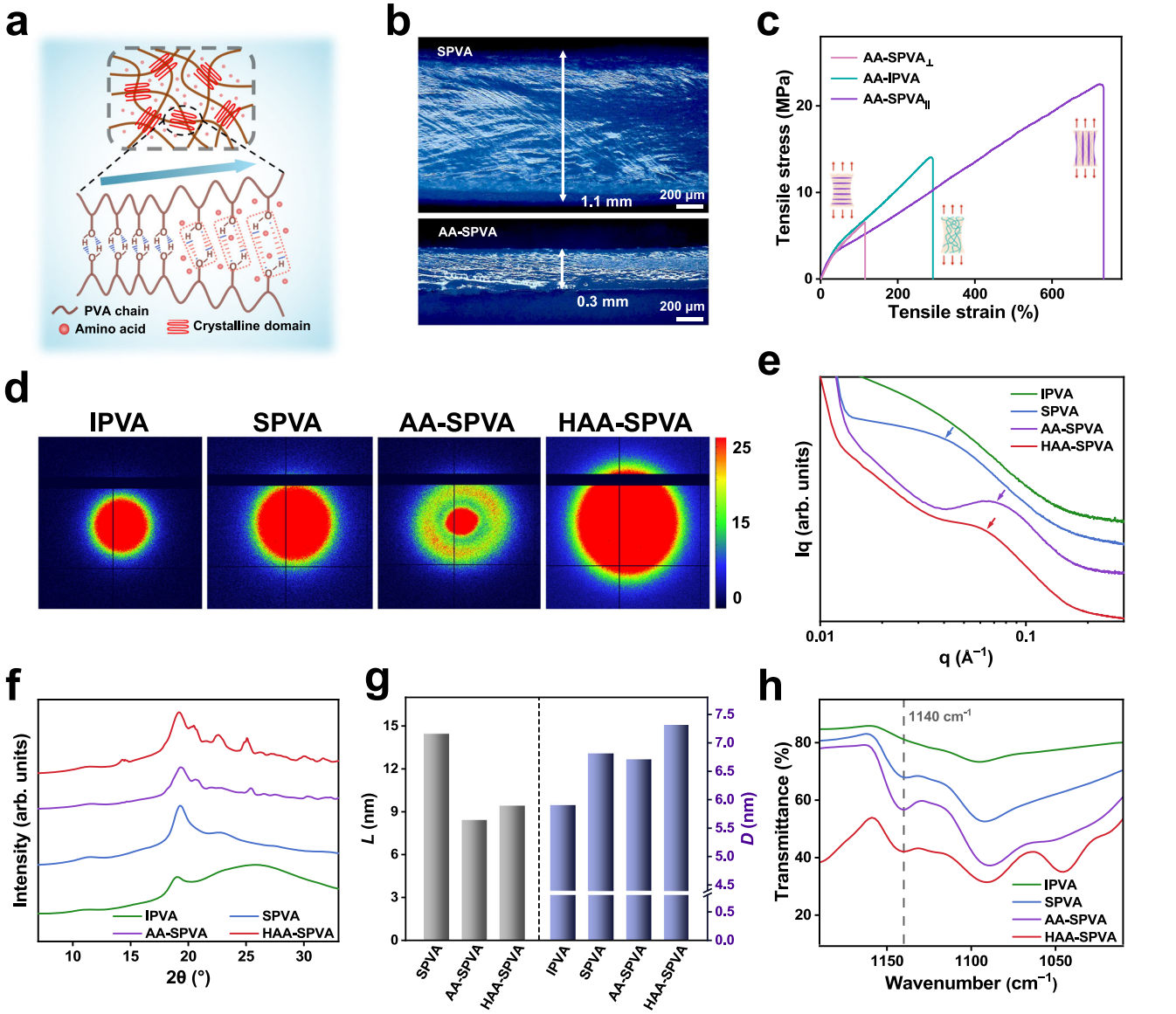

Fig. 4 | Multiscale toughening mechanisms of HAA-SPVA hydrogel. a Formation of hydrogen bonds between PVA chains induced by amino acid. **b** Comparison of the thickness of SPVA rehydrated with water or AA-SPVA rehydrated with amino acid solution. Observation was repeated three times independently, yielding similar results. **c** Tensile stress-strain curves of AA-SPVA hydrogel in the directions parallel (∥) and perpendicular (⊥) to the alignment as well as AA-IPVA hydrogel. **d**–**f** SAXS patterns (**d**), SAXS profiles (**e**), and WAXS profiles (**f**) of IPVA, SPVA, AA-SPVA, and HAA-SPVA hydrogels. **g** The distance between crystalline domains (*L*) and the size of crystalline domain (*D*) of IPVA, SPVA, AA-SPVA, and HAA-SPVA hydrogels. **h** ATR-FTIR spectra of IPVA, SPVA, AA-SPVA, and HAA-SPVA hydrogels.

infiltration (Fig. 5c). From further immunohistochemical staining analysis (Fig. 5c, d), the expression of CD68 (marker for macrophage) and IL-6 (an inflammatory factor) in the HAA-SPVA hydrogel group is comparable to that in the control group receiving sham surgery without implant. Therefore, our HAA-SPVA hydrogel has good biocompatibility both in vitro and in vivo.

To evaluate the bioadhesion of the asymmetric porous surfaces of HAA-SPVA hydrogel, cell adhesion experiment was performed. The reverse-fixed HAA-SPVA (denoted as rHAA-SPVA) hydrogel with its dense porous surface used for seeding fibroblasts, and commercial anti-adhesion Parietex composite (PCO) mesh were set as the control group. As shown in Fig. 5e, f, more L929 fibroblasts are attached to the loose extracellular-matrix-like porous surface of HAA-SPVA hydrogel, while only a few fibroblasts are observed on the dense porous surface of rHAA-SPVA hydrogel and the anti-adhesion PCO mesh. Moreover, the fluorescence staining images show that the cytoskeletons of L929 fibroblasts are more extended in a filamentous arrangement on the loose extracellular-matrix-like porous surface of HAA-SPVA hydrogel than those on its dense porous surface (Supplementary Fig. 16). These results clearly indicate that our HAA-SPVA hydrogel exhibits contradictory bioadhesive properties because of its unique asymmetric porous surfaces.

We further applied HAA-SPVA hydrogel to repair rabbit diaphragm defect to demonstrate its asymmetric bioadhesion and biomechanical support for dynamic tissue repair in vivo (Fig. 6a). The loose porous surface of HAA-SPVA hydrogel was sutured upon the diaphragm with a 10 mm full-thickness defect to promote healing, with the dense porous surface facing the abdominal cavity to prevent visceral adhesion (Supplementary Fig. 17). The rHAA-SPVA hydrogel and commercial anti-adhesion PCO mesh were also applied for comparison. On the 14th day after surgery, no pneumothorax or hernia is observed, demonstrating the stable mechanical support by HAA-SPVA hydrogel. To clarify the anti-adhesion effect, photos of visceral adhesions (Fig. 6b) and corresponding quantitative scorings (Fig. 6c) for

https://doi.org/10.1038/s41467-025-58062-4

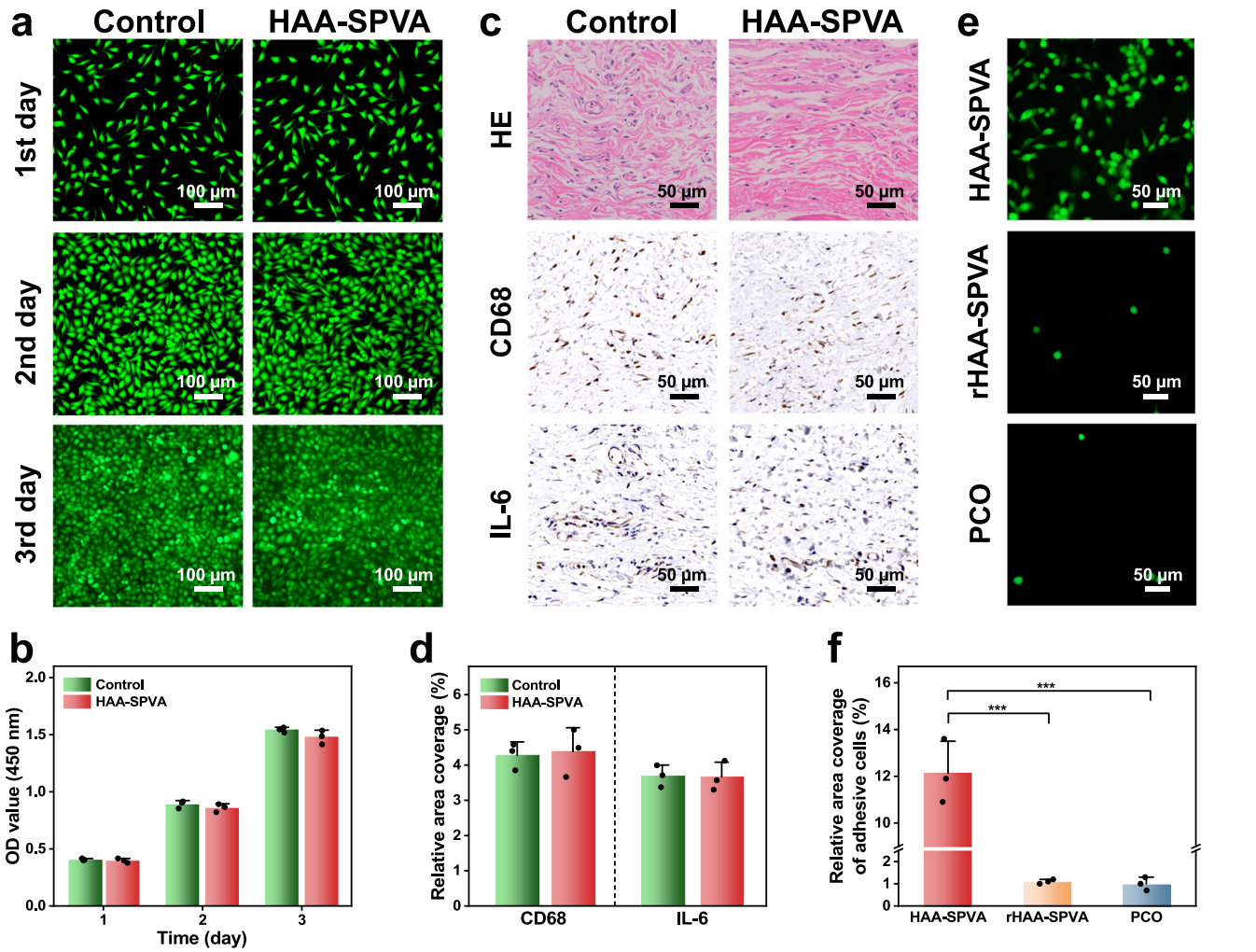

Fig. 5 | Biocompatibility and asymmetric bioadhesive behaviors of HAA-SPVA hydrogel. a, **b** Fluorescence images (**a**) and CCK-8 assay (**b**) of L929 fibroblasts cultured for 1, 2, and 3 days in the control and HAA-SPVA hydrogel groups ($n = 3$ independent samples; Student's t test; two-tailed $P = 0.497$, 0.327, and 0.165 for 1, 2, and 3 days, respectively; error bars = standard deviation (SD); data are presented as mean ± SD). **c** Images of HE staining and immunohistochemical staining of CD68 and IL-6 in the control and HAA-SPVA hydrogel groups after subcutaneous implantation in rats for 14 days. **d** Quantitative analysis of CD68 and IL-6 ($n = 3$ independent samples; Student's t test; two-tailed $P = 0.829$ and 0.934 for CD68 and IL-6, respectively; error bars = SD; data are presented as mean ± SD). **e**, **f** Fluorescence images (**e**) and quantitative analysis (**f**) of L929 fibroblasts incubated on the asymmetric porous surfaces of HAA-SPVA hydrogel and PCO mesh ($n = 3$ independent samples; ANOVA followed by Tukey's multiple comparisons; *** adjusted $P < 0.001$; error bars = SD; data are presented as mean ± SD).

different groups are shown. Minimal visceral adhesion formation is found in the HAA-SPVA hydrogel group with an average adhesion score of 0.6, compared with mild adhesion in the anti-adhesion PCO mesh group with a score of 1.6, and moderate visceral adhesion in the rHAA-SPVA hydrogel group with a score of 5.0, suggesting excellent anti-adhesion effect through the dense porous surface of HAA-SPVA hydrogel. Defect healing was further evaluated with histology on the 14th day (Fig. 6d). Benefiting from its loose porous surface and better tissue compliance, the HAA-SPVA hydrogel group shows more collagen deposition (Fig. 6e) and neovascularization (Fig. 6f) at the site of defects, which demonstrates a higher degree of tissue healing[85]. Therefore, our HAA-SPVA hydrogel has achieved the integration of contradictory tissue adhesion behaviors (i.e., anti-adhesion and pro-healing) and biomechanical support through multiscale structural regulation.

In summary, we have developed a robust super-structured porous hydrogel through a unique directional freezing-assisted progressive solvent exchange method. By further toughening with amino acid, the designed hydrogel mimics multiscale biological prototype of dynamic soft tissues and correspondingly achieves multiple combinations of contradictory properties, including excellent mechanical properties of high strength, stiffness, toughness and fatigue resistance, as well as biological properties of anti-adhesion and pro-healing. Meanwhile, slow mechanical withdrawal through hydrophobic modification enables our hydrogel to provide biomechanical adaptability to meet the needs at different healing phases of tissue defect. Therefore, it is foreseeable that our strategy for strong and tough multiscale biomimetic hydrogels will broaden the prospect for the design and practical application of hydrogels in soft tissue engineering.

Methods

Ethical approval statement

All animal experiments were reviewed and approved by the Animal Ethics Committee of Guangzhou Huateng Biomedical Technology Co., Ltd. (license number: C202302-11 for rats and HTSW23010 for rabbits).

Materials

DMSO (99%), PBS (0.01 M, pH 7.4), and anhydrous ethanol were purchased from Shanghai Macklin Biochemical Technology Co., Ltd. (China). PVA (degree of polymerization ~1700, degree of alcoholysis 98–99 mol%) and L-amino acids (≥99%) were purchased from Shanghai Aladdin Biochemical Technology Co., Ltd. (China). Dodecylboronic

https://doi.org/10.1038/s41467-025-58062-4

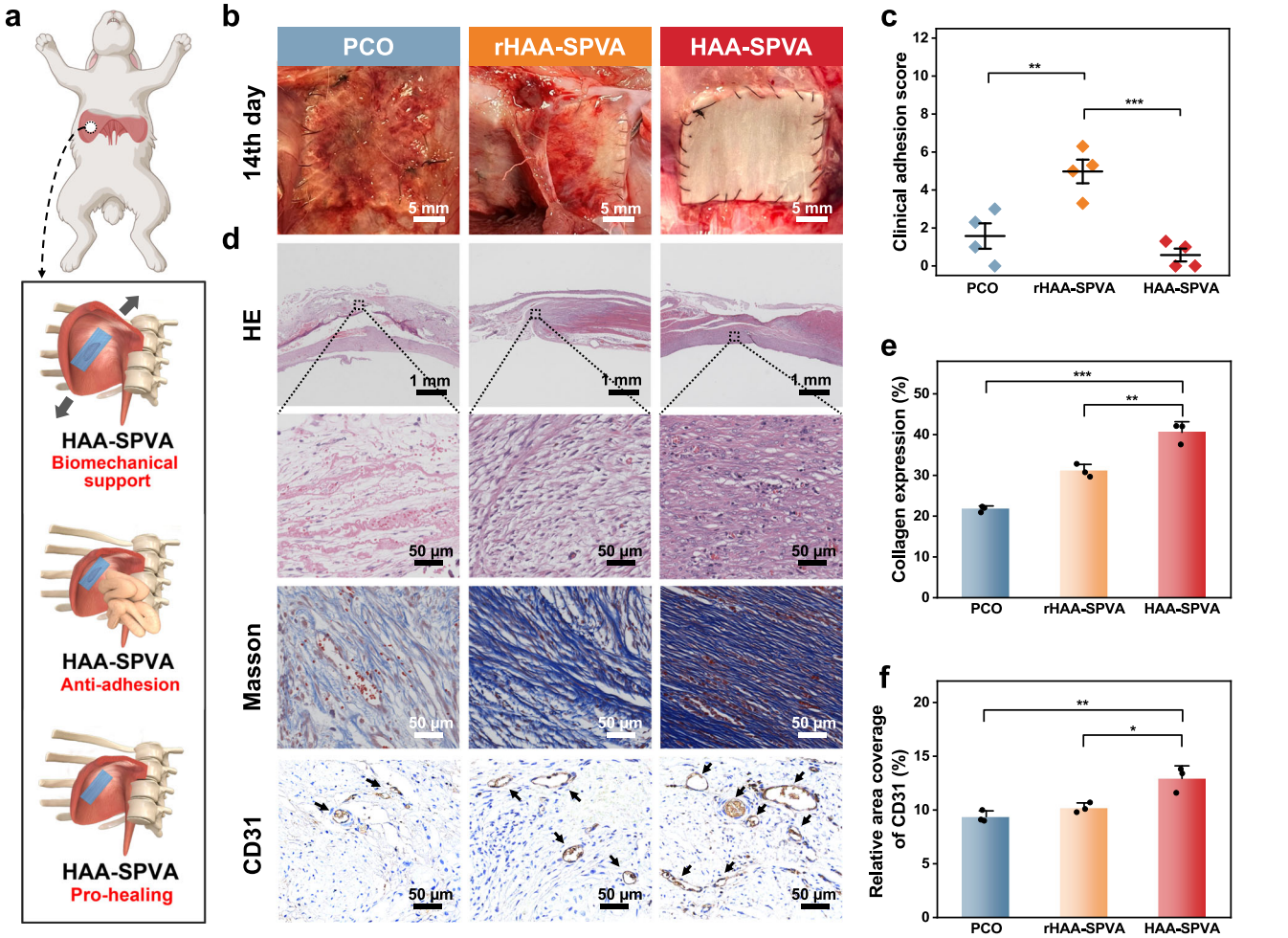

Fig. 6 | Asymmetric bioadhesion and biomechanical support of HAA-SPVA hydrogel in vivo. a Efficacy of HAA-SPVA hydrogel in repairing diaphragm defect in vivo (the rabbit cartoon was created with Biorender.com). **b** The visceral adhesion formation with different treatments (PCO mesh, rHAA-SPVA, and HAA-SPVA hydrogels) on the 14th day after surgery in rabbit diaphragm defect models. **c** Quantitative scoring analysis of clinical visceral adhesion for diaphragm defects with different treatments on the 14th day after surgery ($n = 4$ independent samples; ANOVA followed by Tukey's multiple comparisons; ** adjusted $P = 0.005$, *** adjusted $P < 0.001$; error bars = SD; data are presented as mean ± SD). **d** Images of HE staining, Masson staining, and immunohistochemical staining of CD31 (a vascular endothelial marker). Arrows: microvessels. **e** Quantitative analysis of collagen density ($n = 3$ independent samples; ANOVA followed by Tukey's multiple comparisons; ** adjusted $P = 0.002$, *** adjusted $P < 0.001$; error bars = SD; data are presented as mean ± SD). **f** Quantitative analysis of CD31 ($n = 3$ independent samples; ANOVA followed by Tukey's multiple comparisons; * adjusted $P = 0.013$, ** adjusted $P = 0.004$; error bars = SD; data are presented as mean ± SD).

acid (98%) was purchased from Shanghai Bide Pharmatech Co., Ltd. (China). CCK-8 reagent was purchased from Dojindo Laboratories (Japan). Dulbecco's modified eagle medium (DMEM) was purchased from Gibco BRL Life Technologies, Inc. (USA). Calcein acetoxymethyl ester (calcein-AM) staining kit and 4′,6-diamidino-2-phenylindole (DAPI) were purchased from Shanghai Beyotime Biotech Co., Ltd. (China). 4% paraformaldehyde was purchased from Hefei Biosharp Technology Co., Ltd. (China). Triton X-100 was purchased from Shanghai Sangon Biotech Co., Ltd. (China). Actin-Tracker Green was purchased from Shanghai Yeasen Biotechnology Co., Ltd. (China).

Fabrication of SPVA hydrogel

9 g PVA was dissolved in 50 mL DMSO, stirred at 75 °C for 5 h, and then sonicated for 20 min, yielding clear PVA/DMSO solution. Directional freezing was performed to construct hydrogel with anisotropic structure in a constant-temperature bath at −25 °C. The PVA/DMSO solution was filled into a cuboid tetrafluoroethylene mold, which has a rectangular groove for filling, thick outer walls with thickness of 10 mm for insulation, and a thin bottom with thickness of 2 mm for effective heat transfer. This mold was gradually immersed into the ethanol bath at −25 °C at a rate of 1 mm min^{-1}. Once fully immersed, the anisotropic PVA/DMSO frozen solid was vertically placed along the freezing direction and exposed its top surface to cold moisture for progressive solvent exchange at −20 °C for 24 h, leading to the formation of SPVA organogel. Subsequently, SPVA organogel was immersed in 1 L deionized water for 24 h at room temperature (the water was refreshed every 8 h) and then freeze-dried for 24 h. SPVA hydrogel was obtained by immersing freeze-dried SPVA in deionized water for rehydration.

Fabrication of AA-SPVA hydrogel

The as-prepared freeze-dried SPVA was immersed in various concentrations of L-amino acid aqueous solutions (such as serine, glycine, lysine, arginine, alanine, proline, and cysteine) at room temperature for 5 days for further enhancement of mechanical properties. Among these amino acids, 25 wt% serine solution with a biofriendly pH value was used to develop AA-SPVA hydrogel.

Fabrication of HAA-SPVA hydrogel

A dodecylboronic acid solution was prepared by dissolving 0.7 g dodecylboronic acid powder in 10 mL anhydrous ethanol. AA-SPVA hydrogel was immersed in dodecylboronic acid solution for 100 min at

25 °C for hydrophobization and then soaked in 1 L deionized water for 20 min to obtain HAA-SPVA hydrogel.

Fabrication of IPVA and AA-IPVA hydrogels

The PVA/DMSO solution (9 g PVA in 50 mL DMSO) was poured into the cuboid mold and then directly immersed in 1 L deionized water for 24 h at room temperature (the water was refreshed every 8 h). After freeze-drying for 24 h and rehydration, IPVA hydrogel was obtained. AA-IPVA hydrogel was obtained by immersing freeze-dried IPVA in 25 wt% serine solution at 25 °C for 5 days.

Morphology characterization

The morphology was investigated by field-emission SEM (FE-SEM, S-4800, Hitachi, Japan) and super depth-of-field three-dimensional microscopy (DSX1000, Olympus, Japan). The samples were sectioned along their alignment to reveal cross-sectional areas and treated by freeze-drying for SEM test. The pore size distribution of the samples was measured using the Nano Measurer software (v.1.2.5, Fudan University, China).

Tensile testing

All tensile tests were conducted at room temperature using a universal mechanical testing machine (WD-5A, Guangzhou Experimental Instrument Factory, China) at a stretching speed of 30 mm min^{-1}. The hydrogel samples were cut into dumbbell-shaped pieces with a 2 mm width, and the loading direction was parallel to the alignment structure of hydrogel samples unless otherwise specified. Stress-strain curves were generated by correlating the applied force with the initial cross-sectional area and the displacement with the initial clamp distance. The initial slope of the stress-strain curve was used to determine elastic modulus, and the integrated area under the stress-strain curve was used to determine toughness.

Fatigue testing

The fatigue threshold was assessed using the single-notch technique[30,86]. The testing environment's relative humidity was controlled at about 90% using a humidifier. Notched samples (width 5 mm and initial crack length 1 mm) were cyclically stretched at a prescribed stretch for 5000/10000 cycles with a loading rate of 0.5/1.0 Hz. The stress-strain response under cyclic loading was recorded using an Air servo Fatigue & Endurance Testing Systems (Shimadzu, Japan), and crack propagation of the notched samples was monitored by a digital camera. The energy release rate (G) was calculated using the Eq. (1)[30,86]:

$$G = 2kcW \tag{1}$$

where k is a function varying slowly with strain, represented as $k = 3/\sqrt{\varepsilon+1}$, c refers to the crack length, and W is the strain energy density of unnotched samples with the same dimensions applied to the same strain ε and Nth cycle. The crack growth rate (dc/dN) and G are established by testing at various cyclic strains. The fatigue threshold (Γ_0) can be calculated by linearly extrapolating the curve of dc/dN versus G to the x intercept.

Measurement of swelling ratio

The initial weight of our PVA hydrogels was recorded as w_0. Subsequently, the hydrogel samples were soaked in PBS at 37 °C. After predetermined time, the samples were taken out and wiped with filter paper, and their weight was recorded as w_t. The swelling ratio represented by Δw was calculated using the Eq. (2):

$$\Delta w = \frac{w_t - w_0}{w_0} \times 100\% \tag{2}$$

X-ray scattering

The SAXS and WAXS measurements were conducted using Xeuss 3.0 SAXS/WAXS System (Xenocs, France) with a Eiger2R 1 M detector. The wavelength of X-ray utilized was 0.154 nm with an energy of 30 W. The sample-to-detector distance was established at 500 mm for SAXS and 60 mm for WAXS, covering a momentum transfer (q) range of 0.013–0.521 $Å^{-1}$ for SAXS and diffraction angle (2θ) range of 1.3–46.9° for WAXS. The distance between crystalline domains (L) was calculated using the Bragg Eq. (3)[87]:

$$L = 2\pi/q_{\max} \tag{3}$$

where q_{max} is the vector signifying the peak intensity.

The size of crystalline domain (D) was calculated using the Scherrer's Eq. (4)[88]:

$$D = k\lambda/(\beta\cos\theta) \tag{4}$$

where k is the dimensionless shape factor, assumed to be 1 for spherical crystalline domains, λ is the X-ray diffraction wavelength, θ is the Bragg angle, and β is the full width at half maximum of the peak.

ATR-FTIR characterization

The ATR-FTIR spectral analysis was conducted to examine the vibrations of functional groups of hydrogel samples using a Cary610/670 infrared spectrometer (Agilent, USA).

In vitro biocompatibility

The cytocompatibility of HAA-SPVA hydrogel was evaluated by live/dead and CCK-8 assays. L929 fibroblasts were provided by the National Collection of Authenticated Cell Cultures (Cat. No. GNM28, China). L929 fibroblasts were seeded on 96-well plates with 100 μL DMEM containing 10% fetal bovine serum and 1% penicillin-streptomycin at a density of 3.5×10^3 cells per well, and then incubated in a humidified incubator with 5% CO_2 at 37 °C. After incubation for 24 h, hydrogels were added to each well in the HAA-SPVA hydrogel group. After incubation for 1, 2, and 3 days, the medium was removed, and each well was rinsed three times with PBS. After incubation with calcein-AM (2 μg mL^{-1}) solution for 30 min under dark condition, cell morphology was observed by an inverted fluorescence microscopy. On the other hand, after incubation with 10% CCK-8 reagent under dark condition for 2 h, optical density (OD) values were detected at 450 nm absorbance.

In vivo biocompatibility

Male Sprague-Dawley rats (250–300 g, 7–8 weeks) and female New Zealand rabbits (2–2.5 kg, 3 months) were used for in vivo experiments adhering to strict Laboratory Animal Care and Use Guidelines. Histological staining was conducted by Wuhan Servicebio Technology Co., Ltd (China).

In vivo biocompatibility was evaluated by implanting HAA-SPVA hydrogel into the dorsal subcutaneous tissue of rats. The samples sterilized using ultraviolet irradiation were cut into 1 cm × 1 cm slices and implanted into the incisions of dorsal skin of rats after the anesthesia. Rats in the control group were incised and sutured in the same way as the experimental group, but no material was implanted. On the 14th day after surgery, tissue specimens from the subcutaneous implanted regions were extracted and fixed in 4% paraformaldehyde solution for 24 h for histological staining, including HE staining and immunohistochemical staining with CD68 antibody (1:200, GB113109; ServiceBio, China) and IL-6 antibody (1:800, GB11117; ServiceBio, China).

Cell adhesion test

Cell adhesion test was performed to understand the bioadhesion of the asymmetrical porous surfaces of HAA-SPVA hydrogel by using live/dead assay. Samples were cut into 8 mm diameter slices, placed on a 48-well plate, and sterilized by ultraviolet irradiation for 2 h. L929 fibroblasts at the density of 2×10^4 cells per well were seeded on the asymmetric porous surfaces of HAA-SPVA hydrogel and the anti-adhesion surface of commercial PCO mesh. After incubation for 48 h, each well was rinsed 3 times with PBS, and the hydrogels and meshes were moved to a new 48-well plate for cell staining. L929 cells on the surface of samples were stained with a calcein-AM solution of 2 μg mL^{-1} for 30 min at 37 °C and then examined by an inverted fluorescence microscopy. For further observation of morphology, the samples were fixed by 4% paraformaldehyde and permeabilized in 0.5% Triton X-100. Cells on the samples were stained with Actin-Tracker Green and DAPI and then visualized by a confocal laser scanning microscope (CLSM; LSM880 NLO, Zeiss, Germany).

Diaphragm defect repair experiment in rabbit

The asymmetric bioadhesion and biomechanical support of HAA-SPVA hydrogel were evaluated by diaphragm defect repair experiments on New Zealand rabbits. The rabbits received an intravenously pentobarbital dose (30 mg kg^{-1}) for anesthesia followed by endotracheal intubation. Throughout the surgery, anesthesia was sustained with 1%–3% isoflurane in oxygen. A sterile transverse incision was made under the left rib for abdominal cavity access. A 10 mm diameter full-thickness diaphragmatic defect was excised on the left hemi-diaphragm. The defects were repaired with HAA-SPVA hydrogel, rHAA-SPVA hydrogel, and PCO mesh, all of which were sutured with 5-0 braided threads. The transverse incisions were closed with 3-0 silk braided threads. On the 14th day after surgery, humane euthanasia was performed on the rabbits. After a new incision was made along the original incision to access the repair site, visceral adhesion and defect healing were evaluated and photographed. In addition, the clinical adhesion scoring criteria was used to assess the severity of visceral adhesion (Supplementary Table 2)[89–91]. Tissue specimens from the repaired regions were extracted and fixed in 4% paraformaldehyde solution for 24 h. Histological staining, including HE staining, Masson staining, and immunohistochemical staining with CD31 antibody (1:50, NB600-562; Novus, USA) was conducted.

Statistical analysis

Statistical analyses were executed using SPSS (v.27.0.1.0, IBM Corporation, USA). Data were presented as mean ± standard deviation. The student's *t* test or a one-way analysis of variance (ANOVA) followed by Tukey's multiple comparisons for data with homogeneity of variance was performed for determining statistical significance. The histological results were quantitatively analyzed by Image J (v.1.53t, National Institutes of Health, USA). Levels of statistical significance were denoted as * $P < 0.05$, ** $P < 0.01$, and *** $P < 0.001$.

Reporting summary

Further information on research design is available in the Nature Portfolio Reporting Summary linked to this article.

Data availability

Data supporting the results of this study are available in the paper and its Supplementary Information. All data underlying this study are accessible from the corresponding authors upon request. Source data are provided with this paper.

References

1. Moroni, L. et al. Biofabrication strategies for 3D in vitro models and regenerative medicine. *Nat. Rev. Mater.* **3**, 21–37 (2018).
2. Nepal, D. et al. Hierarchically structured bioinspired nanocomposites. *Nat. Mater.* **22**, 18–35 (2023).
3. Raman, R. Modeling muscle. *Science* **363**, 1051–1051 (2019).
4. Hua, M. et al. Strong tough hydrogels via the synergy of freeze-casting and salting out. *Nature* **590**, 594–599 (2021).
5. Liu, Z., Meyers, M. A., Zhang, Z. & Ritchie, R. O. Functional gradients and heterogeneities in biological materials: Design principles, functions, and bioinspired applications. *Prog. Mater. Sci.* **88**, 467–498 (2017).
6. Wegst, U. G. K., Bai, H., Saiz, E., Tomsia, A. P. & Ritchie, R. O. Bioinspired structural materials. *Nat. Mater.* **14**, 23–36 (2015).
7. Martinez-Lemus, L. A. The Dynamic Structure of Arterioles. *Basic Clin. Pharmacol. Toxicol.* **110**, 5–11 (2012).
8. Komuro, T. & Hashimoto, Y. Three-dimensional structure of the rat intestinal wall (Mucosa and submucosa). *Arch. Histol. Cytol.* **53**, 1–21 (1990).
9. Cao, J. & Poss, K. D. The epicardium as a hub for heart regeneration. *Nat. Rev. Cardiol.* **15**, 631–647 (2018).
10. Orabi, H. et al. Tissue Engineering of Urinary Bladder and Urethra: Advances from Bench to Patients. *Sci. World J.* **2013**, 154564 (2013).
11. Lessa, T. B., de Abreu, D. K., Bertassoli, B. M. & Ambrósio, C. E. Diaphragm: A vital respiratory muscle in mammals. *Ann. Anat. - Anat. Anz.* **205**, 122–127 (2016).
12. Gasser, T. C., Ogden, R. W. & Holzapfel, G. A. Hyperelastic modelling of arterial layers with distributed collagen fibre orientations. *J. R. Soc. Interface* **3**, 15–35 (2006).
13. Guimarães, C. F., Gasperini, L., Marques, A. P. & Reis, R. L. The stiffness of living tissues and its implications for tissue engineering. *Nat. Rev. Mater.* **5**, 351–370 (2020).
14. Filippidi, E. et al. Toughening elastomers using mussel-inspired iron-catechol complexes. *Science* **358**, 502–505 (2017).
15. Li, X. & Gong, J. P. Design principles for strong and tough hydrogels. *Nat. Rev. Mater.* **9**, 380–398 (2024).
16. Ritchie, R. O. The conflicts between strength and toughness. *Nat. Mater.* **10**, 817–822 (2011).
17. Ma, P. et al. Super-Structured Wet-Adhesive Hydrogel with Ultralow Swelling, Ultrahigh Burst Pressure Tolerance, and Anti-Postoperative Adhesion Properties for Tissue Adhesion. *Adv. Mater.* **36**, 2305400 (2024).
18. Wang, H. et al. An Integrally Formed Janus Hydrogel for Robust Wet-Tissue Adhesive and Anti-Postoperative Adhesion. *Adv. Mater.* **35**, 2300394 (2023).
19. Wiegand, C. & White, R. Microdeformation in wound healing. *Wound Repair Regen.* **21**, 793–799 (2013).
20. Strodtbeck, F. Physiology of wound healing. *Newborn Infant Nurs. Rev.* **1**, 43–52 (2001).
21. Harn, H. I.-C. et al. The tension biology of wound healing. *Exp. Dermatol.* **28**, 464–471 (2019).
22. Jaiswal, D. et al. Tendon tissue engineering: biomechanical considerations. *Biomed. Mater.* **15**, 052001 (2020).
23. Seliktar, D. Designing Cell-Compatible Hydrogels for Biomedical Applications. *Science* **336**, 1124–1128 (2012).
24. Wang, Z., Wei, H., Huang, Y., Wei, Y. & Chen, J. Naturally sourced hydrogels: emerging fundamental materials for next-generation healthcare sensing. *Chem. Soc. Rev.* **52**, 2992–3034 (2023).
25. Zhao, X. et al. Soft Materials by Design: Unconventional Polymer Networks Give Extreme Properties. *Chem. Rev.* **121**, 4309–4372 (2021).
26. Zhang, K., Feng, Q., Fang, Z., Gu, L. & Bian, L. Structurally Dynamic Hydrogels for Biomedical Applications: Pursuing a Fine Balance between Macroscopic Stability and Microscopic Dynamics. *Chem. Rev.* **121**, 11149–11193 (2021).
27. Hassan, C. M. & Peppas, N. A. Structure and Morphology of Freeze/Thawed PVA Hydrogels. *Macromolecules* **33**, 2472–2479 (2000).

28. Xu, L. et al. A Solvent-Exchange Strategy to Regulate Noncovalent Interactions for Strong and Antiswelling Hydrogels. *Adv. Mater.* **32**, 2004579 (2020).
29. Wu, S. et al. Poly(vinyl alcohol) Hydrogels with Broad-Range Tunable Mechanical Properties via the Hofmeister Effect. *Adv. Mater.* **33**, 2007829 (2021).
30. Lin, S. et al. Anti-fatigue-fracture hydrogels. *Sci. Adv.* **5**, eaau8528 (2019).
31. Mredha, Md. T. I. & Jeon, I. Biomimetic anisotropic hydrogels: Advanced fabrication strategies, extraordinary functionalities, and broad applications. *Prog. Mater. Sci.* **124**, 100870 (2022).
32. Zhao, H. et al. Multiscale engineered artificial tooth enamel. *Science* **375**, 551–556 (2022).
33. Bao, B. et al. Rapid fabrication of physically robust hydrogels. *Nat. Mater.* **22**, 1253–1260 (2023).
34. Ajdary, R., Tardy, B. L., Mattos, B. D., Bai, L. & Rojas, O. J. Plant Nanomaterials and Inspiration from Nature: Water Interactions and Hierarchically Structured Hydrogels. *Adv. Mater.* **33**, 2001085 (2021).
35. Zhao, Z., Fang, R., Rong, Q. & Liu, M. Bioinspired Nanocomposite Hydrogels with Highly Ordered Structures. *Adv. Mater.* **29**, 1703045 (2017).
36. Takahashi, N., Kanaya, T., Nishida, K. & Kaji, K. Effects of cononsolvency on gelation of poly(vinyl alcohol) in mixed solvents of dimethyl sulfoxide and water. *Polymer* **44**, 4075–4078 (2003).
37. Wu, S. et al. Rapid and scalable fabrication of ultra-stretchable, anti-freezing conductive gels by cononsolvency effect. *EcoMat* **3**, e12085 (2021).
38. Mayer, S., Metzger, R. & Kluth, D. The embryology of the diaphragm. *Semin. Pediatr. Surg.* **20**, 161–169 (2011).
39. Ugalde, P. A., Pereira, S. T., Araujo, C. & Irion, K. L. Correlative Anatomy for the Mediastinum. *Thorac. Surg. Clin.* **21**, 251–272 (2011).
40. Guo, X., Dong, X., Zou, G., Gao, H. & Zhai, W. Strong and tough fibrous hydrogels reinforced by multiscale hierarchical structures with multimechanisms. *Sci. Adv.* **9**, eadf7075 (2023).
41. Zhang, Z. et al. Fatigue-Resistant Conducting Polymer Hydrogels as Strain Sensor for Underwater Robotics. *Adv. Funct. Mater.* **33**, 2305705 (2023).
42. Liang, X. et al. Bioinspired 2D Isotropically Fatigue-Resistant Hydrogels. *Adv. Mater.* **34**, 2107106 (2022).
43. Liang, X. et al. Anisotropically Fatigue-Resistant Hydrogels. *Adv. Mater.* **33**, 2102011 (2021).
44. Zhao, Y. et al. Somatosensory actuator based on stretchable conductive photothermally responsive hydrogel. *Sci. Robot.* **6**, eabd5483 (2021).
45. Feng, Y. et al. Muscle-Inspired MXene Conductive Hydrogels with Anisotropy and Low-Temperature Tolerance for Wearable Flexible Sensors and Arrays. *Adv. Funct. Mater.* **31**, 2105264 (2021).
46. Zhao, Y. et al. Hierarchically Structured Stretchable Conductive Hydrogels for High-Performance Wearable Strain Sensors and Supercapacitors. *Matter* **3**, 1196–1210 (2020).
47. Kong, P. et al. Extracellular Matrix/Glycopeptide Hybrid Hydrogel as an Immunomodulatory Niche for Endogenous Cardiac Repair after Myocardial Infarction. *Adv. Sci.* **10**, 2301244 (2023).
48. Krishtul, S., Baruch, L. & Machluf, M. Processed Tissue–Derived Extracellular Matrices: Tailored Platforms Empowering Diverse Therapeutic Applications. *Adv. Funct. Mater.* **30**, 1900386 (2020).
49. Pappu, R. V., Cohen, S. R., Dar, F., Farag, M. & Kar, M. Phase Transitions of Associative Biomacromolecules. *Chem. Rev.* **123**, 8945–8987 (2023).
50. de With, G. Melting Is Well-Known, but Is It Also Well-Understood? *Chem. Rev.* **123**, 13713–13795 (2023).
51. Jungwirth, P. & Cremer, P. S. Beyond Hofmeister. *Nat. Chem.* **6**, 261–263 (2014).
52. Zhang, Y., Furyk, S., Bergbreiter, D. E. & Cremer, P. S. Specific Ion Effects on the Water Solubility of Macromolecules: PNIPAM and the Hofmeister Series. *J. Am. Chem. Soc.* **127**, 14505–14510 (2005).
53. Gonzalez, A. C. et al. Wound healing - A literature review. *Bras. Dermatol.* **91**, 614–620 (2016).
54. Wu, W. et al. Mechanostructures: Rational mechanical design, fabrication, performance evaluation, and industrial application of advanced structures. *Prog. Mater. Sci.* **131**, 101021 (2023).
55. Doneva, M. & Pashkouleva, D. Investigation of mechanical compatibility of hernia meshes and human abdominal fascia. *Biomed. Mater. Eng.* **29**, 147–158 (2018).
56. Afzali Naniz, M., Bodaghi, M., Safar Johari, M. & Zolfagharian, A. Influence of Hybridization on Tensile Behaviors of Non-Absorbable Braided Polymeric Sutures. *Polymers* **12**, 682 (2020).
57. de Cesare, N., Trevisan, C., Maghin, E., Piccoli, M. & Pavan, P. G. A finite element analysis of diaphragmatic hernia repair on an animal model. *J. Mech. Behav. Biomed. Mater.* **86**, 33–42 (2018).
58. Zhang, Q. et al. 3D Printed High-Strength Supramolecular Polymer Hydrogel-Cushioned Radially and Circumferentially Oriented Meniscus Substitute. *Adv. Funct. Mater.* **32**, 2200360 (2022).
59. Mredha, Md. T. I. et al. A Facile Method to Fabricate Anisotropic Hydrogels with Perfectly Aligned Hierarchical Fibrous Structures. *Adv. Mater.* **30**, 1704937 (2018).
60. Xu, L. et al. Conjoined-network rendered stiff and tough hydrogels from biogenic molecules. *Sci. Adv.* **5**, eaau3442 (2019).
61. Li, W. et al. Nanoconfined polymerization limits crack propagation in hysteresis-free gels. *Nat. Mater.* **23**, 131–138 (2024).
62. Wu, Y. et al. Solvent-Exchange-Assisted Wet Annealing: A New Strategy for Superstrong, Tough, Stretchable, and Anti-Fatigue Hydrogels. *Adv. Mater.* **35**, 2210624 (2023).
63. Wu, J. et al. Strong and Ultra-Tough Supramolecular Hydrogel Enabled by Strain-Induced Microphase Separation. *Adv. Funct. Mater.* **33**, 2210395 (2023).
64. Xue, B. et al. Strong, tough, rapid-recovery, and fatigue-resistant hydrogels made of picot peptide fibres. *Nat. Commun.* **14**, 2583 (2023).
65. Wang, M. et al. Tough and stretchable ionogels by in situ phase separation. *Nat. Mater.* **21**, 359–365 (2022).
66. Li, W. et al. Tough Hydrogels with Isotropic and Unprecedented Crack Propagation Resistance. *Adv. Funct. Mater.* **32**, 2207348 (2022).
67. Zhang, M. et al. Toughening Double-Network Hydrogels by Polyelectrolytes. *Adv. Mater.* **35**, 2301551 (2023).
68. Kobielarz, M., Kozuń, M., Gąsior-Głogowska, M. & Chwiłkowska, A. Mechanical and structural properties of different types of human aortic atherosclerotic plaques. *J. Mech. Behav. Biomed. Mater.* **109**, 103837 (2020).
69. Cunnane, E. M., Barrett, H. E., Kavanagh, E. G., Mongrain, R. & Walsh, M. T. The influence of composition and location on the toughness of human atherosclerotic femoral plaque tissue. *Acta Biomater.* **31**, 264–275 (2016).
70. Deeken, C. R. & Lake, S. P. Mechanical properties of the abdominal wall and biomaterials utilized for hernia repair. *J. Mech. Behav. Biomed. Mater.* **74**, 411–427 (2017).
71. Bourgouin, S. et al. Biomechanical characterisation of fresh and cadaverous human small intestine: applications for abdominal trauma. *Med. Biol. Eng. Comput.* **50**, 1279–1288 (2012).
72. Liu, X. et al. Fatigue-resistant hydrogel optical fibers enable peripheral nerve optogenetics during locomotion. *Nat. Methods* **20**, 1802–1809 (2023).
73. Lin, S., Liu, J., Liu, X. & Zhao, X. X. Muscle-like fatigue-resistant hydrogels by mechanical training. *Proc. Natl Acad. Sci.* **116**, 10244–10249 (2019).

74. Ni, J. et al. Strong fatigue-resistant nanofibrous hydrogels inspired by lobster underbelly. *Matter* **4**, 1919–1934 (2021).
75. Liu, P., Zhang, Y., Guan, Y. & Zhang, Y. Peptide-Crosslinked, Highly Entangled Hydrogels with Excellent Mechanical Properties but Ultra-Low Solid Content. *Adv. Mater.* **35**, 2210021 (2023).
76. Li, W. et al. Recyclable, Healable, and Tough Ionogels Insensitive to Crack Propagation. *Adv. Mater.* **34**, 2203049 (2022).
77. Taylor, D., O'Mara, N., Ryan, E., Takaza, M. & Simms, C. The fracture toughness of soft tissues. *J. Mech. Behav. Biomed. Mater.* **6**, 139–147 (2012).
78. Gillies, A. R. & Lieber, R. L. Structure and function of the skeletal muscle extracellular matrix. *Muscle Nerve* **44**, 318–331 (2011).
79. Sun, X., Mao, Y., Yu, Z., Yang, P. & Jiang, F. A Biomimetic "Salting Out—Alignment—Locking" Tactic to Design Strong and Tough Hydrogel. *Adv. Mater.* **36**, 2400084 (2024).
80. Xu, L., Qiao, Y. & Qiu, D. Coordinatively Stiffen and Toughen Hydrogels with Adaptable Crystal-Domain Cross-Linking. *Adv. Mater.* **35**, 2209913 (2023).
81. Li, W. et al. Supramolecular Ionogels Tougher than Metals. *Adv. Mater.* **35**, 2301383 (2023).
82. Jomova, K. et al. Essential metals in health and disease. *Chem. Biol. Interact.* **367**, 110173 (2022).
83. Song, P. et al. Granular Nanostructure: A Facile Biomimetic Strategy for the Design of Supertough Polymeric Materials with High Ductility and Strength. *Adv. Mater.* **29**, 1704661 (2017).
84. Chen, B. et al. Giant negative thermopower of ionic hydrogel by synergistic coordination and hydration interactions. *Sci. Adv.* **7**, eabi7233 (2021).
85. Weingarten, M. S. et al. Correlation of near infrared absorption and diffuse reflectance spectroscopy scattering with tissue neovascularization and collagen concentration in a diabetic rat wound healing model. *Wound Repair Regen.* **16**, 234–242 (2008).
86. Long, R. & Hui, C.-Y. Fracture toughness of hydrogels: measurement and interpretation. *Soft Matter* **12**, 8069–8086 (2016).
87. Zhang, R. et al. Stretch-induced complexation reaction between poly(vinyl alcohol) and iodine: an in situ synchrotron radiation small- and wide-angle X-ray scattering study. *Soft Matter* **14**, 2535–2546 (2018).
88. Patterson, A. L. The Scherrer Formula for X-Ray Particle Size Determination. *Phys. Rev.* **56**, 978–982 (1939).
89. Kobayashi, N. et al. Impacts of pleural adhesions on lobectomies for malignant lung tumors. *Gen. Thorac. Cardiovasc. Surg.* **70**, 1042–1047 (2022).
90. Hwang, H. J. et al. All the commercially available adhesion barriers have the same effect on adhesion prophylaxis?; A comparison of barrier agents using a newly developed, severe intra-abdominal adhesion model. *Int. J. Colorectal Dis.* **28**, 1117–1125 (2013).
91. Shin, C. S. et al. 3D-Bioprinted Inflammation Modulating Polymer Scaffolds for Soft Tissue Repair. *Adv. Mater.* **33**, 2003778 (2021).

Acknowledgements

The authors acknowledge financial support from the National Natural Science Foundation of China (51925308, D.W.; 22271320, R.H.), the Guangdong Major Project of Basic and Applied Basic Research (2023B0303000025, D.W.), the Fundamental Research Funds for the Central Universities, Sun Yat-sen University (23yxqntd002, D.W.), the Science and Technology Planning Project of Guangdong Province (2021B1212040017, D.W.), the Science and Technology Development Fund, Macau S.A.R (0004/2021/AKP, R.D.), the Medical Scientific and Technical Foundation of Guangdong Province (A2023085, W.L.), the Guangdong Basic Research Center of Excellence for Functional Molecular Engineering, the National Key Clinical Discipline (D.W.), and the Start-up Foundation of Recruited Talents of the Eighth Affiliated Hospital of Sun Yat-sen University (GCCRCYJ041, D.W.).

Author contributions

D.W., R.D., and R.H. supervised the project. D.W., R.H., and W.L. conceived the underlying idea. R.D., S.H., W.L., and Y.T. designed the research and carried out the experiments. S.H., J.Z., R.W., L.Q., and Y.O. performed the statistical analysis. S.H., W.L., and Y.T. wrote the manuscript. All the authors contributed to discussing and revising the manuscript.

Competing interests

The authors declare no competing interests.

Additional information

Supplementary information The online version contains supplementary material available at https://doi.org/10.1038/s41467-025-58062-4.

Correspondence and requests for materials should be addressed to Rongkang Huang, Ruoxu Dou or Dingcai Wu.

Peer review information *Nature Communications* thanks the anonymous reviewer(s) for their contribution to the peer review of this work. A peer review file is available.